

1 Vertical structure of biomass burning aerosol transported over 2 the southeast Atlantic Ocean

3 Harshvardhan Harshvardhan¹, Richard Ferrare², Sharon Burton², Johnathan Hair², Chris
4 Hostetler², David Harper², Anthony Cook², Marta Fenn³, Amy Jo Scarino³, Eduard Chemyakin³,
5 Detlef Müller⁴

6 ¹Department of Earth, Atmospheric and Planetary Sciences, Purdue University, West Lafayette, IN, United States

7 ²NASA Langley Research Center, Hampton, VA, United States

8 ³Science Systems and Applications, Inc./NASA Langley Research Center, Hampton, VA, United States

9 ⁴Department of Physics, Astronomy and Mathematics, University of Hertfordshire, Hatfield, Hertfordshire, United
10 Kingdom

11 *Correspondence to:* H. Harshvardhan (harshvar@purdue.edu)

12 **Abstract.** Biomass burning in southwestern Africa produces smoke plumes that are transported over the Atlantic
13 Ocean and overlie vast regions of stratocumulus clouds. This aerosol layer contributes to direct and indirect radiative
14 forcing of the atmosphere in this region, particularly during the months of August, September and October. There was
15 a multi-year international campaign to study this aerosol and its interactions with clouds. Here we report on the
16 evolution of aerosol distributions and properties as measured by the airborne high spectral resolution lidar (HSRL-2)
17 during the ORACLES (Observations of Aerosols above Clouds and their intERactionS) campaign in September 2016.
18 The NASA Langley HSRL-2 instrument was flown on the NASA ER-2 aircraft for several days in September 2016.
19 Data were aggregated at two pairs of 2°×2° grid boxes to examine the evolution of the vertical profile of aerosol
20 properties during transport over the ocean. Results showed that the structure of the profile of aerosol extinction and
21 microphysical properties is maintained over a one to two-day time scale. In the 3-5 km altitude range, 95% of the
22 aerosol extinction was contributed by particles in the 0.05-0.50 μm radius size range, with the aerosol in this size
23 range having an average effective radius of 0.16 μm. This indicates that there is essentially no scavenging or dry
24 deposition at these altitudes. Moreover, there is very little day to day variation in these properties, such that time
25 sampling as happens in such campaigns, may be representative of longer periods such as monthly means. Below 3 km
26 there is considerable mixing with larger aerosol, most likely continental source near land. Furthermore, these
27 measurements indicated that there was often a distinct gap between the bottom of the aerosol layer and cloud tops at
28 the selected locations as evidenced by a layer of several hundred meters that contained relatively low aerosol extinction
29 values above the clouds.

30 1 Introduction

31 Aerosols are often considered as the most confounding element in the climate system when simulating parameters of
32 the Earth's current climate. Their interaction with clouds makes the problem extremely complicated. The general topic
33 of aerosol-cloud interaction has been of great interest in the scientific community: to quote the report of the

34 Intergovernmental Panel on Climate Change (IPCC AR5) “Clouds and aerosols continue to contribute the largest
35 uncertainty to estimates and interpretations of the Earth’s changing energy budget” (Boucher et al., 2013).

36 In the context of these interactions, the interplay of biomass burning (BB) aerosol and the stratocumulus clouds in
37 the Southeast (SE) Atlantic is unique and crucial to the estimates of the energy budget of the region. This BB aerosol
38 arises from the seasonal burning (July-October) of agricultural residue in the southwestern African Savannah and
39 traverses large distances westward over the SE Atlantic Ocean. Unlike the aerosol from industrial activity and biofuels
40 that intermingle with clouds in many regions (Ramanathan et al., 2001; Mechoso et al., 2013), these optically thick
41 BB aerosol layers overlay vast stretches of marine stratus cloud in the SE Atlantic (Chand et al., 2009; Wilcox, 2010;
42 Adebisi et al., 2020) where they have a direct radiative effect. The BB aerosol can also act as nuclei for cloud droplets
43 and so cause a potentially significant cloud albedo effect. Observations and modelling studies of such interactions in
44 the Southeast Atlantic and southern Africa regions include Diamond et al. (2018), Kacarab et al. (2020), Mallet et al.
45 (2020) and Gupta et al. (2022). There is also some evidence that aerosol can alter the thermodynamics of cloud
46 formation through semi-direct effects (Sakaeda et al., 2011). Studies using high resolution limited area models have
47 shown a variety of effects, including stratus to cumulus transition resulting from these interactions (Yamaguchi et al.,
48 2015; Gordon et al., 2018; Lu et al., 2018). The semi-direct effect has also been shown to be important in a limited
49 time run of a global model (Das et al., 2020).

50 During the course of its transport over the Atlantic basin, the dense BB aerosol layer affects the underlying clouds
51 and Earth’s radiative balance in multiple ways. It exerts a direct radiative forcing (DRF) by scattering and absorbing
52 solar radiation in the atmosphere; when clouds are present, these aerosols absorb incoming solar radiation along with
53 the radiation reflected by the underlying cloud surface (Chand et al., 2009; Meyer et al., 2013; Zhang et al., 2016).
54 Simultaneously, depending on the relative vertical location of the aerosol with respect to the cloud deck, the cloud
55 cover (fraction) or liquid water path may increase or decrease in response to heating of surrounding air masses due to
56 aerosol absorption and subsequent changes in atmospheric stability — the semi-direct forcing (Sakaeda et al., 2011;
57 Wilcox, 2012; Das et al., 2020). Observations at Ascension Island show that daytime cloud cover and relative humidity
58 are lower when there is more smoke in the marine boundary layer (Zhang and Zuidema, 2019). Moreover, as the
59 marine boundary layer (MBL) deepens farther offshore and north of 5° S, subsiding aerosol particles become entrained
60 into the MBL and interact with the clouds as cloud condensation nuclei to affect their microphysics (indirect forcing)
61 (Costantino and Breon, 2013; Painemal et al., 2014).

62 In the context of simulating the above alluded aerosol radiative effects, it is vital that aerosol-cloud overlap
63 characteristics are accurately represented within the models. The quantification of these aerosol-cloud overlap
64 characteristics in the models is necessary for a variety of reasons. For example, previous studies have found that the
65 sign and magnitude of DRF of absorbing aerosol above clouds (AAC) critically depends upon the reflectance and
66 coverage of the underlying cloud surfaces along with the optical properties, composition and size distribution of the
67 overlying aerosols (Keil and Haywood, 2003; Chand et al., 2009). Additionally, the magnitude and sign of the aerosol
68 semi-direct effects are quite sensitive to the vertical distribution of aerosols, especially with respect to the vertical
69 location of clouds (Penner et al., 2003; McFarquhar and Wang, 2006; Koch and Del Genio, 2010).

70 Here we address the evolution of the vertical properties of BB aerosol as it travels in the marine environment after
71 leaving the African land mass. Section 2 identifies the field campaign and specifies the geographic region selected for
72 the analysis and rationale for that choice. Section 3 describes the attributes of the instrument and key parameters
73 related to the aerosol that can be extracted from the measurements. Section 4 presents the results followed by a
74 summary and conclusion in section 5.

75 **2 Field Campaigns**

76 The concerns mentioned above were the driving force behind plans for several international multi-year field
77 campaigns; ORACLES (Observations of Aerosols above Clouds and their intEractionS, Redemann et al., 2021),
78 CLARIFY-2017 (CLOUD-Aerosol-Radiation Interactions and Forcing for Year 2017, Haywood et al., 2021), and
79 LASIC (Layered Atlantic Smoke Interactions with Clouds, Zuidema et al., 2016, 2018). A key component of the
80 September 2016 NASA ORACLES Intensive Observation Period (IOP) was the vertical profiling of aerosol properties
81 measured by an airborne lidar, the NASA Langley High Spectral Resolution Lidar-2, HSRL-2 (Burton et al., 2018),
82 on-board the NASA ER-2, which was based in Walvis Bay, Namibia, for operations during 2016, the deployment
83 covered in this study. In the following two years, the instrument was on-board the P-3 flying out of São Tomé. The
84 siting and flight tracks chosen ensured adequate coverage of the seasonal BB aerosol.

85 **2.1 Meteorology**

86 The September monthly mean meteorological situation is shown in Fig. 1 from MERRA-2 (Modern-Era
87 Retrospective analysis for Research and Applications, version 2) reanalysis (Buchard et al., 2017; Randles et al., 2017)
88 along with locations of relevant sites. A thorough meteorological analysis for all ORACLES deployments is provided
89 in Ryoo et al. (2021). For the period under consideration here, they found that the African Easterly Jet-South (AEJ-
90 S), fast moving zonal easterlies centered on 650 hPa around 5-15°S, was active and corresponded closely to the long-
91 term climatology. Fig. 2 shows 650 hPa winds from MERRA-2 reanalysis at the beginning, at the end, and on two
92 intermediate days during which HSRL-2 measurements were made. ER-2 flight tracks during the September 2016
93 IOP are shown in Fig. 3. Note that flights were primarily confined to within roughly 1000 km of the African coast
94 with only the 22 September flight venturing further. Flights such as executed during the IOP are unable to follow air
95 parcels in a Lagrangian fashion to examine the evolution of smoke plumes. Here we provide an alternate framework
96 by which to study evolving aerosol properties in an average sense. In order to establish average characteristics of the
97 BB smoke plume as it travels over the ocean, we have chosen five grid boxes of two-degree latitude and longitude on
98 a side at various distances from the source and aggregated observations. The choice of grid boxes was based on the
99 availability of data from the flights (Fig. 3) and the general direction of transport of the smoke as evidenced by the
100 wind fields in Fig. 2. The grid boxes so chosen are marked on Figs. 2 and 3 and the rationale for the choice is explained
101 below.

102 Figure 4 shows 48-hour backward trajectory frequency analyses at 3.5 km, roughly the central altitude of the plume,
103 using NOAA HYSPLIT (Hybrid Single-Particle Lagrangian Integrated Trajectory) trajectory calculations
104 (https://www.ready.noaa.gov/HYSPLIT_traj.php, last accessed September 18, 2021) which were carried out using
105 archived GDAS (Global Data Assimilation System) 0.5-degree meteorology (Stein et al., 2015). The frequency
106 distribution is a 48-hour history of the paths taken by air parcels arriving at the grid boxes marked A and C at 3500 m
107 altitude. The time period of the frequency analyses covers the entire period during which HSRL-2 measurements were
108 made, 12-24 September 2016. The selected grid box pairs indicate that Box A receives aerosol that has earlier crossed
109 Box B and Box C is downwind of Box D; boxes B and D receive aerosol directly from BB sources on land. The grid
110 box pairs A/B and C/D can therefore provide information on the evolution of the microphysics and vertical distribution
111 of BB aerosol plumes after leaving the continent. This strategy is similar to that used in comparisons of models with
112 observations for this campaign by Shinozuka et al. (2020), who also showed that observations made on the sampled
113 days were representative of monthly means. In addition to the four boxes strongly influenced by smoke, a southern
114 box, E, has been chosen to provide a control contrast to the other areas in that it is influenced primarily by maritime
115 air as seen from Figs. 1 and 2.

116 2.2 ORACLES 2016 IOP

117 The days during the campaign that were included in the averaging procedure are shown in Table 1. Also included
118 is the typical time of the day when the measurements were made, a function of the flight pattern of the ER-2. The
119 number of lidar return profiles averaged for each grid box and statistics related to the backward trajectories are also
120 listed. These grid boxes contained aircraft tracks on multiple days during which trajectory analysis showed near-
121 uniform wind direction between 2.5 and 4.5 km altitude throughout the IOP. With the exception of the grid box
122 centered at 22° S, 9° E, all indicate flow from the source region of BB aerosol. Table 1 also lists the mean and standard
123 deviation of time duration in hours spent over water of air parcels arriving at 3500 m altitude at the grid box during
124 the averaging period. There is no entry for Box E since arriving air had a maritime source and did not originate from
125 land. It must be stressed that the duration is not calculated from the source region on land, which is distributed over a
126 large area of central Africa (e.g., Fig. 9 of Redemann et al., 2021) and cannot be uniquely identified with specific
127 observations made over the ocean. The plume has already been airborne over land for several hours (see Fig. 4) and
128 aerosol would have undergone transformations that occur at short time scales (Cappa et al., 2020). The duration was
129 calculated by running HYSPLIT backward trajectories of air parcels arriving every six hours starting at 0600 UTC on
130 the days of the first flight and ending at 1800 UTC on the days of the last flight of the averaging period and is shown
131 in some detail in Fig. 5, which essentially reflects the profile of the prevailing wind speeds. The inference is that BB
132 smoke at 3500 m altitude arrives at A on average about 30 h after passing B and arrives at C 35 h after passing D. The
133 change in selected aerosol properties as measured by the HSRL-2 during this travel in the marine environment provides
134 information on the evolution of the plume during this time period.

135

136 3 HSRL-2

137 The NASA LaRC (Langley Research Center) HSRL-2 uses the HSRL technique to independently retrieve aerosol
138 extinction and backscatter (Shipley et al., 1983; Grund and Eloranta, 1991; She et al., 1992) without a priori
139 assumptions on aerosol type or extinction-to-backscatter ratio. By using the HSRL technique, HSRL-2, like its
140 predecessor HSRL-1 (Hair et al., 2008), provides accurate backscatter profiles even in situations where the lidar beam
141 is attenuated by overlying cloud or aerosol as long as it is not completely attenuated. The LaRC HSRL-2 employs the
142 HSRL technique at 355 and 532 nm and the standard backscatter technique at 1064 nm. It also measures aerosol and
143 cloud depolarization at all three wavelengths. The HSRL-2 provides vertically resolved measurements of the following
144 extensive and intensive aerosol parameters below the aircraft (approximate archival horizontal, Δx , and vertical
145 resolutions, Δz , are listed assuming ER-2 cruise speed).

146 • *Extensive parameters*¹ – backscatter coefficient, β , at 355, 532 and 1064 nm ($\Delta x \sim 2$ km, $\Delta z \sim 15$ m); extinction
147 coefficient, α , at 355, and 532 nm ($\Delta x \sim 12$ km, $\Delta z \sim 300$ m); optical depth at 355 and 532 nm (integrating the profile
148 of extinction). The aerosol optical depth (AOD) is a critical quantity in discussions of the influence of aerosol on
149 climate (Boucher et al., 2013).

150 • *Intensive parameters* – extinction-to-backscatter ratio of aerosol, the Lidar Ratio, $S_a = \alpha_a / \beta_a$, at 355 and 532 nm
151 ($\Delta x \sim 12$ km, $\Delta z \sim 300$ m); depolarization, $\delta_a = \beta_a^\perp / \beta_a^\parallel$, at 355, 532, and 1064 nm ($\Delta x \sim 2$ km, $\Delta z \sim 15$ m); and
152 aerosol backscatter wavelength dependence (i.e., Ångström exponent for aerosol backscatter – directly related to the
153 backscatter color ratio) for two wavelength pairs (355-532 and 532-1064 nm, $\Delta x \sim 2$ km, $\Delta z \sim 15$ m).

154 The overall systematic error associated with the backscatter calibration is estimated to be less than 5 % for the 355
155 and 532 nm channels and 20 % for 1064 nm (Burton et al., 2015). Under typical conditions, the total systematic error
156 for extinction is estimated to be less than 0.01 km^{-1} at 532 nm. The random errors for all aerosol products are typically
157 less than 10 % for the backscatter and depolarization ratios (Hair et al., 2008). Rogers et al. (2009) validated the HSRL
158 extinction coefficient profiles and found that the HSRL extinction profiles are within the typical state-of-the-art
159 systematic error at visible wavelengths (Schmid et al., 2006). Since HSRL-2 includes the capability to measure
160 backscatter at three wavelengths and extinction at two wavelengths, “ $3\beta+2\alpha$ ” microphysical retrieval algorithms
161 (Müller et al., 1999a, 1999b; Veselovskii et al., 2002) are used to retrieve height-resolved parameters such as aerosol
162 effective radius and number, surface and volume concentrations (Müller et al., 2014, Sawamura et al., 2017). Here we
163 restrict ourselves to the effective radius of the particles.

164

¹ By the term *extensive*, we refer to optical parameters, such as extinction, that are influenced by the amount (concentration) and type (size, composition, shape) of aerosol/cloud particles. *Intensive* properties, on the other hand, are those that depend only on the nature of the particles and not on their quantity or concentration, but rather depend only on aerosol type (Anderson et al., 2003).

165 4 Results

166 In this study of the vertically resolved evolving properties of BB aerosol, we present key lidar measurements and
167 microphysical results obtained by performing the “ $3\beta+2\alpha$ ” retrieval mentioned in Section 3.

168 4.1 Lidar

169 Vertical profiles averaged over the times of overflight in $2^\circ \times 2^\circ$ latitude/longitude boxes shown in Figure 3 on the
170 days given in Table 1 are for the following properties.

- 171 1. Aerosol extinction at 532 nm, α_a , determined by aerosol number concentration, microphysical
172 properties and relative humidity
- 173 2. Backscatter Ångström exponent between 1064 and 532 nm, an indication of particle size.
- 174 3. Aerosol depolarization at 532 nm, a measure of particle asphericity.
- 175 4. The lidar ratio (ratio of aerosol extinction to backscatter) at 532 nm, a marker for aerosol composition.

176 Inspection of the wind field at 650 hPa in Fig. 2 and backward trajectory frequency plots in Fig. 4 suggest that the
177 grid boxes chosen fit naturally into two pairs of tracks of the widespread BB aerosol field. The northern pair, identified
178 in Table 1 as A and B, centered around 10° S, are in a faster zonal track, whereas the grid boxes C and D are in a track
179 centered between $13\text{--}15^\circ$ S that is slightly slower and has a component from the north over a stretch of water (Fig. 2).
180 The two pairs can then provide information on the evolution of aerosol properties over a time scale of one to two days.
181 Figures 6-9 show the aerosol extinction, backscatter Ångström exponent, aerosol depolarization and Lidar Ratio for
182 the two pairs of grid boxes and Box E, which is at the southern edge of the region influenced by the BB aerosol. The
183 results presented are one-minute averages of independent 10 s vertical profiles for backscatter Ångström exponent
184 and depolarization and one-minute averages for extinction and lidar ratio profiles. From Table 1, the mean time elapsed
185 between B and A is 29.4 h and that between D and C is 34.9 h. It should be pointed out that parameter values shown
186 below the level of mean cloud top are averages of lidar returns through breaks in the stratus deck and are not relevant
187 for this study. If we use the low cut-off of an extinction coefficient of 15 Mm^{-1} to indicate an aerosol-free layer
188 (Shinozuka et al., 2020), then Fig. 6 indicates that the bulk of the smoke layers encountered at these distances from
189 land were separated from the cloud top, a feature more prevalent during the 2016 IOP than in 2017 and 2018
190 (Redemann et al., 2021).

191 The northern plume is a column of aerosol of relatively constant extinction from just above 2.5 km to 5 km while
192 the southern plume has a profile of extinction that increases nearly linearly with height from a minimum near the cloud
193 top to a maximum at 5 km (Fig. 6). The vertical structure of the aerosol profiles measured by HSRL-2 was compared
194 to water vapor profiles represented by the MERRA-2 model. Pistone et al. (2021) explored the relationship between
195 aerosols, CO, water vapor as measured by ORACLES airborne in situ measurements and represented by models
196 including MERRA-2. They found the MERRA-2 water vapor profiles, like the measured water vapor profiles,
197 exhibited a linear relationship with CO and biomass burning plume strength; they also found that smoky, humid air
198 produced by daytime convection over the continent advected over the ocean and into the ORACLES study region.

199 MERRA-2 water vapor profiles produced at three hourly increments and 72 pressure levels were interpolated to the
200 times and locations of the HSRL-2 profiles. Water vapor mixing ratio generally decreased significantly just above the
201 PBL then increased for altitudes around 2 to 3 km before decreasing again. This behavior is generally consistent with
202 the relationship between water vapor and aerosol scattering reported by Pistone et al. (2021).

203 Figure 10 shows the median, 25th and 75th percentile relative humidity (RH) profiles computed by interpolating the
204 MERRA-2 0.5-deg. 3-hourly humidity profiles to the locations and times of the HSRL-2 measurements. The profiles
205 typically show a more pronounced increase in RH with altitude that more closely follows the HSRL-2 measurements
206 of aerosol extinction profiles, although the MERRA-2 profiles typically begin decreasing above 4 km whereas the
207 airborne in situ RH measurements and HSRL-2 aerosol extinction profiles begin decreasing above 5 km. Interestingly,
208 during three of the dates (Sept. 12, 16, 22) considerable portions of the smoke layers correspond to MERRA-2 relative
209 humidity above 60-70%. This increase in RH with altitude could help explain at least some of the increase in aerosol
210 extinction with height observed in the HSRL-2 profiles of the C/D Box pair. Aerosol humidification often amplified
211 the increase in aerosol extinction by factors of 1.5 or more (Doherty et al., 2022).

212 The Ångström exponent (Fig. 7) and depolarization (Fig. 8) indicate the presence of fine spherical particles at the
213 top of the plume and increasing sizes towards the bottom. The Lidar Ratio (Fig. 9) above 3 km for the two pairs is
214 between 70 and 80 sr, suggesting strong absorption (Müller et al., 2019) but is considerably less and highly variable
215 in Box E and in the lower layers of the aerosol plume in Box D, where the smoke plume most likely has components
216 of continental aerosol such as dust and pollution typical of the nearby Namibian coast (Klopper et al., 2020). The most
217 striking feature of the results is the very small profile-to-profile variability of the intensive lidar parameters in the
218 upper two kilometers of the plume over the course of several days as evident from the range of values in the 25-75
219 percentile shaded grey in Figs. 7-9. This suggests strongly that the particles maintain their size, shape and absorbing
220 properties over the first few days of transport over the ocean. This result is of some importance for climate studies in
221 which the radiative properties of BB aerosol are input to the calculation of radiative forcing. Complex chain aggregates
222 as found near the source of fires (Pósfai et al., 2003, China et al., 2013) are typically not represented in climate models.
223 However, if the aerosol is already spherical and maintains its size over the time period of radiative interactions being
224 studied, then core-shell models of varying degrees of complexity could perhaps suffice (Zhang et al., 2020). The lower
225 portion of the plume containing larger BB aerosol particles is subject to mixing with marine and continental particles
226 from regions not affected by biomass burning and is highly variable in nature. This would be more difficult to model
227 but Fig. 6 shows that the aerosol extinction coefficient decreases rapidly at lower levels so errors in representation
228 may be acceptable.

229 **4.2 Microphysics**

230 The lidar measurements are inverted to obtain information regarding particle size. The inversion is performed on one-
231 minute averages of six independent 10 s backscatter profiles and one-minute average extinction profiles. Details of
232 the inversion process are in Müller et al. (2019) and references therein. The particle size distribution is represented
233 using a series of eight triangular basis functions that can represent both monomodal and bimodal size distributions

234 (*ibid*). Points to note are that the procedure makes the following assumptions: the particles are spherical and
235 homogeneous having wavelength-independent complex index of refraction. The low ($< 5\%$) values of depolarization
236 through most of the plume, shown in Fig. 8, suggests that the spherical assumption is justified. There is most likely
237 structure and inhomogeneity in the core of the particles, but current particle optical models are unable to incorporate
238 these complexities. Results from this inversion procedure have been compared to coincident airborne in situ particle
239 measurements. Müller et al. (2014) present results from a campaign off the northeast coast of the US showing that the
240 inversion results agree with in situ measurements of effective radius and also number, surface area and volume
241 concentration within error bars. Sawamura et al. (2017) report on campaigns in the wintertime San Joaquin Valley of
242 California and summertime near Houston, TX. They found high correlation and low bias in surface and volume
243 concentration in situ measurements relative to HSRL with the best agreement for submicron fine-mode aerosol, which
244 is most relevant to the current study. Müller et al. (2019) report retrievals and their uncertainty for one day in the
245 ORACLES campaign, 22 September 2016. Considering only optical data with strong signal-to-noise ratio, they
246 estimate retrieval errors are 25 % for number concentration. The relative uncertainty in effective radius for parts of
247 the flight track where particle size was nearly constant was below 20 %.

248 In order to help separate particles that have BB source from coarser particles of continental or marine origin, we
249 specify a Submicron Fraction (SMF) as the contribution to the extinction at 532 nm of particles in the radius range
250 0.05–0.50 μm (Anderson et al., 2005). Figure 11 shows the profiles of SMF for the five grid boxes and not surprisingly,
251 the bulk of the smoke plume, especially between 3 and 5 km contains aerosol almost entirely in the submicron range.
252 Below 3 km, at locations both near and further way from the coast, there is a marked increase in the fraction of larger
253 particles. The increase in depolarization (Fig. 8) at these lower levels and a decrease in the Lidar Ratio (Fig. 9) suggest
254 mixing with the aforementioned non-BB aerosol particles. However, the sharp decrease in extinction below 3 km (Fig.
255 6) indicates that their contribution to direct radiative effects would be minimal. Finally, Fig. 12 shows the vertical
256 profile of the effective radius of the SMF aerosol population. The effective radius is 0.16 μm with little variation
257 between 3 and 5 km. Of greater significance is that it remains very similar between the pairs of grid boxes along the
258 transport trajectory of the smoke. The retrieved effective radius is similar to the results presented by Müller et al.
259 (2014) for a mixture of urban aerosol and smoke. Their comparison with in situ measurements showed a slight
260 overestimate but within a standard deviation. The retrieved and in situ results also show that the particle size is uniform
261 with altitude even when the number concentration drops by a factor of three. Another set of prior comparisons of
262 HSRL-2 and in situ measurements is provided in Sawamura et al. (2017). Here again, the effective radius of the
263 submicron fraction of particles, 0.15 μm , is uniform with altitude, and comparable though biased slightly low
264 compared to in situ observations.

265 The effective radii of the SMF aerosols, which typically vary between 0.15 to 0.20 μm , are generally consistent
266 with the sizes reported previously for smoke aerosol in the ORACLES region. Haywood et al. (2021) provide a
267 composite of the aerosol sizes for biomass burning aerosol off the South African coast. These size distributions, which
268 were derived from airborne in situ measurements (Haywood et al., 2003; Peers et al., 2019; Wu et al., 2020), typically
269 correspond to SMF aerosol effective radii between 0.14–0.17 μm and were for the dry aerosol. Shinozuka et al. (2020)
270 reported on airborne aerosol sizes measured during ORACLES by an Ultra-High-Sensitivity-Aerosol Spectrometer

271 (UHSAS) deployed on the NASA P-3 aircraft. The UHSAS measured particles with dry diameters between 60 and
272 1000 nm. SMF aerosol effective radii derived from the UHSAS measurements of volume mean diameter were
273 generally around 0.09-0.10 μm for the dry aerosol. Shinozuka et al. (2020) noted that the UHSAS measurements were
274 somewhat undersized and so were adjusted to account for this effect; this adjustment improved scattering closure with
275 coincident nephelometer measurements. As discussed in section 4.1, the RH on some days was above 60-70% so that
276 effective radii under ambient conditions could be expected to be somewhat higher than for the dry aerosol. Using
277 measurements from an airborne Differential Aerosol Sizing and Hygroscopicity Spectrometer Probe (DASH-SP),
278 Shingler et al. (2016) quantified the size-resolved growth factors for several aerosol types; they found that at RH~70-
279 80%, particle diameters for biomass burning aerosols were about 15-20% larger than for the dry aerosol. Xu et al.
280 (2021) derived aerosol properties during the 2016 ORACLES mission using an inversion algorithm that combined
281 HSRL-2 and Research Scanning Polarimeter (RSP) remote sensing measurements. These retrieved aerosol properties
282 were then compared with those derived from the UHSAS measurements described by Shinozuka et al. (2020). For
283 measurements acquired on Sept. 12, 2016, the SMF aerosol effective radius derived from the remote sensing
284 measurements were generally between 0.12-0.15 μm and were only slightly (0.012 μm) higher than the effective radii
285 for the (dry) SMF aerosol derived from the UHSAS measurements. This suggests that some of this difference is
286 associated with differences in RH between the remote sensing retrievals and the in situ measurements.

287 **5 Conclusions**

288 The results of the aggregated HSRL-2 profiles during the 2016 ORACLES IOP presented here show two main
289 findings. These are however limited to a brief period in the transport of BB smoke from continental Africa over marine
290 clouds in the Atlantic Ocean. This is a limitation of the 2016 campaign because the flight tracks remained within 1000
291 km of the coast. For the period of one to two days after crossing the land-ocean boundary, the fraction of all particles
292 that are in the submicron range in the main smoke plume between 3 and 5 km is around 95 %. The effective radius of
293 the submicron particles in this altitude interval is 0.16 μm and essentially constant with altitude. The particle size is
294 comparable to measured particle sizes in previous campaigns that sampled aerosol that was a mixture of urban haze
295 and smoke (Müller et al., 2014; Sawamura et al., 2017). Moreover, the shape of the median vertical profile of
296 extinction does not change during the first two days of transport over water suggesting the absence of dry deposition
297 and wet scavenging. The low (< 0.05) depolarization ratio of the submicron particles signifies that they are well coated
298 and the assumption of sphericity in the inversion procedure and models that estimate the radiative effects of aerosol
299 is justified. The BB aerosol mix with continental and marine aerosol at the base of the plume but during the September
300 2016 IOP this layer of mixed aerosol tended to have very low extinction coefficients suggesting low abundance and
301 there was often a distinct gap between the plume and the cloud tops.

302 The HSRL-2 instrument was also deployed in the 2017 and 2018 ORACLES campaigns but was deployed on the
303 NASA P-3 which often flew at low altitude to acquire in situ measurements of aerosols and clouds. Consequently, the
304 HSRL-2 was not able to make continuous measurements of the BB aerosol plumes in a manner similar as when
305 deployed on the ER-2. However, there are segments of the track that can provide similar information to the data

306 obtained in the 2016 campaign but for a different time period. Moreover, some flight tracks extended much further
307 from land (Doherty et al., 2021). Analysis of the later campaigns will provide information on the physical evolution
308 of aerosol that has aged for a longer period than is covered in this study.

309 **Data Management**

310 HSRL-2 optical data and retrieved inversion data are available at the NASA archive site
311 <https://espoarchive.nasa.gov/archive/browse/oracles/id8/ER2> and are permanently archived at
312 doi:10.5067/SUBORBITAL/ORACLES/ER2/2016_V1.

313 **Acknowledgements**

314 The lead author would like to thank NASA Langley Research Center for hosting him during a sabbatical when this
315 study was initiated. HSRL-2 participation in ORACLES was supported by NASA through the Earth Venture
316 Suborbital-2 (EVS-2) program (grant no. 13-EVS2-13-0028). Funding for this work was also provided by NASA
317 through the Radiation Sciences Program. We wish to thank the NASA ER-2 pilots and ground crew for their extensive
318 support during ORACLES.

319

320 **References**

321 Anderson, T. L., Charlson, R. J., Winker, D. M., Ogren, J. A., and Holmén, K.: Mesoscale variations of tropospheric
 322 aerosols, *J. Atmos. Sci.*, 60(1), 119-136, 2003.

323 Anderson, T. L., Wu, Y., Chu, D. A., Schmid, B., Redemann, J., and Dubovik, O.: Testing the MODIS satellite
 324 retrieval of aerosol fine-mode fraction, *J. Geophys. Res.*, 110, D18204, doi:10.1029/2005JD005978, 2005.

325 Adebisi, A. A., Zuidema, P., Chang, I., Burton, S. P., and Cairns, B.: Mid-level clouds are frequent above the Southeast
 326 Atlantic stratocumulus clouds, *Atmos. Chem. Phys.*, 20, 11025-11043, doi:10.5194/acp-20-11025-2020, 2020.

327 Boucher, O., Randall, D., Artaxo, P., Bretherton, C., Feingold, G., Forster, P., Kerminen, V.-M., Kondo, Y., Liao, H.,
 328 Lohmann, U., Rasch, P., Satheesh, S. K., Sherwood, S., Stevens, B., and Zhang X.Y.: Clouds and Aerosols. In:
 329 *Climate Change 2013: The Physical Science Basis. Contribution of Working Group I to the Fifth Assessment Report*
 330 *of the Intergovernmental Panel on Climate Change [Stocker, T. F., Qin, D., Plattner, G.-K., Tignor, M., Allen, S.*
 331 *K., Boschung, J., Nauels, A., Xia, Y., Bex V., and Midgley, P. M. (eds.)]. Cambridge University Press, pp. 571-*
 332 *657, doi:10.1017/CBO9781107415324.016, 2013.*

333 Buchard, V., Randles, C. A., da Silva, A. M., Darmenov, A., Colarco, P. R., Govindaraju, R., Ferrare, R. A., Hair, J.,
 334 Beyersdorf, A. J., Ziemba L. D., and Yu, H.: The MERRA-2 aerosol reanalysis, 1980 onwards Part II: Evaluation
 335 and case studies, *J. Climate*, 30, 6851-6871, doi:10.1175/JCLI-D-16-0613.1, 2017.

336 Burton, S. P., Hostetler, C. A., Cook, A. L., Hair, J. W., Seaman, S., Scola, S., Harper, D. B., Smith, J. A., Fenn, M
 337 A., Ferrare, R. A., Saide, P. E., Chemyakin, E. V., and Müller, D.: Calibration of a high spectral resolution lidar
 338 using a Michelson interferometer with data examples from ORACLES, *Appl. Optics*, 57, 6061-6075, 2018.

339 Burton, S. P., Hair, J. W., Kahnert, M., Ferrare, R. A., Hostetler, C. A., Cook, A. L., Harper, D. B., Berkoff, T. A.,
 340 Seaman, S. T., Collins, J. E., Fenn, M. A., and Rogers, R. R.: Observations of the spectral dependence of linear
 341 particle depolarization ratio of aerosols using NASA Langley airborne High Spectral Resolution Lidar, *Atmos.*
 342 *Chem. Phys.*, 15, 13453–13473, doi.org/10.5194/acp-15-13453-2015, 2015.

343 Cappa, C. D., Lim, C. Y., Hagan, D. H., Coggon, M., Koss, A., Sekimoto, K., de Gouw, J., Onasch, T. B., Warneke,
 344 C., and Kroll, J. H.: Biomass-burning-derived particles from a wide variety of fuels – Part 2: Effects of
 345 photochemical aging on particle optical and chemical properties, *Atmos. Chem. Phys.*, 20, 8511-8532,
 346 doi:10.5194/acp-20-8511-2020, 2020.

347 Chand, D., Wood, R., Anderson, T. L., Satheesh, S. K., and Charlson, R. J.: Satellite-derived direct radiative effect of
 348 aerosols dependent on cloud cover, *Nat. Geosci.*, 2, 181-184, doi:10.1038/Ngeo437, 2009.

349 China, S., Mazzoleni, C., Gorkowski, K., Aiken, A. C., and Dubey, M. K.: Morphology and mixing state of individual
 350 freshly emitted wildfire carbonaceous particles, *Nat. Commun.*, 4:2122 doi: 10.1038/ncomms3122, 2013.

351 Costantino, L., and Bréon F. M.: Aerosol indirect effect on warm clouds over South-East Atlantic from co-located
 352 MODIS and CALIPSO observations, *Atmos. Chem. Phys.*, 13, 69-88, doi:10.5194/acp-13-69-2013, 2013.

353 Das, S., Harshvardhan, H., and Colarco, P. R.: The influence of elevated smoke layers on stratocumulus clouds over
 354 the SE Atlantic in the NASA Goddard Earth Observing System (GEOS) Model, *J. Geophys. Res. Atmos.*, 125,
 355 e2019JD031209. doi:10.1029/2019JD031209, 2020.

356 Diamond, M. S., Dobracki, A., Freitag, S., Small Griswold, J. D., Heikkila, A., Howell, S. G., Kacarab, M. E.,
 357 Podolske, J. R., Saide, P. E., and Wood, R.: Time-dependent entrainment of smoke presents an observational
 358 challenge for assessing aerosol–cloud interactions over the southeast Atlantic Ocean, *Atmos. Chem. Phys.*, 18,
 359 14623–14636, https://doi.org/10.5194/acp-18-14623-2018, 2018.

360 Doherty, S. J., Saide, P. E., Zuidema, P., Shinozuka, Y., Ferrada, G. A., Gordon, H., Mallet, M., Meyer, K.,
 361 Painemal, D., Howell, S. G., Freitag, S., Dobracki, A., Podolske, J. R., Burton, S. P., Ferrare, R. A., Howes, C.,
 362 Nabat, P., Carmichael, G. R., da Silva, A., Pistone, K., Chang, I., Gao, L., Wood, R., and Redemann, J.: Modeled
 363 and observed properties related to the direct aerosol radiative effect of biomass burning aerosol over the Southeast
 364 Atlantic, *Atmos. Chem. Phys.*, 22, 1-46, https://doi.org/10.5194/acp-22-1-2022, 2022.

365 Gordon, H., Field, P. R., Abe, S. J., Dalvi, M., Grosvenor, D. P., Hill, A. A., Johnson, B. T., Miltenberger, A. K.,
 366 Yoshioka, M., and Carslaw, K. S.: Large simulated radiative effects of smoke in the south-east Atlantic, *Atmos.*
 367 *Chem. Phys.*, 18, 15261-15289, doi:10.5194/acp-18-15261-2018, 2018.

368 Grund, C. J., and Eloranta, E. W.: University of Wisconsin high spectral resolution lidar, *Opt. Eng.*, 30, 6-12, 1991.

369 Gupta, S., McFarquhar, G. M., O'Brien, J. R., Poellot, M. R., Delene, D. J., Miller, R. M., and Small Griswold, J. D.:
 370 Factors affecting precipitation formation and precipitation susceptibility of marine stratocumulus with variable
 371 above- and below-cloud aerosol concentrations over the Southeast Atlantic, *Atmos. Chem. Phys.*, 22, 2769-2793,
 372 <https://doi.org/10.5194/acp-22-2769-2022>, 2022.

373 Hair, J. W., Hostetler, C. A., Cook, A. L., Harper, D. B., Ferrare, R. A., Mack, T. L., Welch, W., Izquierdo, L. R.,
374 Hovis, F. E.: Airborne High Spectral Resolution Lidar for profiling aerosol optical properties, *Appl. Optics*, 47,
375 6734-6752, doi:10.1364/AO.47.006734, 2008.

376 Haywood, J. M., Osborne, S. R., Francis, P. N., Keil, A., Formenti, P., Andreae, M. O., and Kaye, P. H.: The mean
377 physical and optical properties of regional haze dominated by biomass burning aerosol measured from the C-130
378 aircraft during SAFARI 2000, *J. Geophys. Res.*, 108, 8473, <https://doi.org/10.1029/2002JD002226>, 2003.

379 Haywood, J. M., Abel, S. J., Barrett, P. A., Bellouin, N., Blyth, A., Bower, K. N., Brooks, M., Carslaw, K., Che, H.,
380 Coe, H., Cotterell, M. I., Crawford, I., Cui, Z., Davies, N., Dingley, B., Field, P., Formenti, P., Gordon, H., de
381 Graaf, M., Herbert, R., Johnson, B., Jones, A. C., Langridge, J. M., Malavelle, F., Partridge, D. G., Peers, F.,
382 Redemann, J., Stier, P., Szpek, K., Taylor, J. W., Watson-Parris, D., Wood, R., Wu, H., and Zuidema, P.: The
383 CLOUD–Aerosol–Radiation Interaction and Forcing: Year 2017 (CLARIFY-2017) measurement campaign, *Atmos.*
384 *Chem. Phys.*, 21, 1049–1084, <https://doi.org/10.5194/acp-21-1049-2021>, 2021.

385 Kacarab, M., Thornhill, K. L., Dobracki, A., Howell, S. G., O'Brien, J. R., Freitag, S., Poellot, M. R., Wood, R.,
386 Zuidema, P., Redemann, J., and Nenes, A.: Biomass burning aerosol as a modulator of the droplet number in the
387 southeast Atlantic region, *Atmos. Chem. Phys.*, 20, 3029–3040, <https://doi.org/10.5194/acp-20-3029-2020>, 2020.

388 Keil, A., and Haywood, J. M.: Solar radiative forcing by biomass burning aerosol particles during SAFARI 2000: A
389 case study based on measured aerosol and cloud properties, *J. Geophys. Res. Atmos.*, 108, 8467,
390 doi:10.1029/2002JD002315, 2003.

391 Klopper, D., Formenti, P., Namwoonde, A., Cazaunau, M., Chevaillier, S., Feron, A., Gaimoz, C., Hease, P., Lahmidi,
392 F., Mirande-Bret, C., Triquet, S., Zeng, Z., and Piketh, S. J.: Chemical composition and source apportionment of
393 atmospheric aerosols on the Namibian coast, *Atmos. Chem. Phys.*, 20, 15,811-15,833, doi:10.5194/acp-20-15811-
394 2020, 2020.

395 Koch, D., and Del Genio A. D.: Black carbon semi-direct effects on cloud cover: review and synthesis, *Atmos. Chem.*
396 *Phys.*, 10, 7685-7696, doi:10.5194/acp-10-7685-2010, 2010.

397 Lu, Z., Liu, X., Zhang, Z., Zhao, C., Meyer, K., Rajapakshe, C., Wu, C., Yang, Z., and Penner, J.: Biomass smoke
398 from southern Africa can significantly enhance the brightness of stratocumulus over the southeastern Atlantic
399 Ocean, *Proc. Natl. Acad. Sci.*, 115, 2924-2929, doi:10.1073/pnas.1713703115, 2018.

400 Mallet, M., Solmon, F., Nabat, P., Elguindi, N., Waquet, F., Bouniol, D., Sayer, A. M., Meyer, K., Roehrig, R.,
401 Michou, M., Zuidema, P., Flaant, C., Redemann, J., and Formenti, P.: Direct and semi-direct radiative forcing of
402 biomass-burning aerosols over the southeast Atlantic (SEA) and its sensitivity to absorbing properties: a regional
403 climate modeling study, *Atmos. Chem. Phys.*, 20, 13191-13216, <https://doi.org/10.5194/acp-20-13191-2020>, 2020.

404 McFarquhar, G. M., and Wang, H.: Effects of aerosols on trade wind cumuli over the Indian Ocean: Model
405 simulations, *Q. J. R. Meteorol. Soc.*, 132, 821-843, doi:10.1256/qj.04.179, 2006.

406 Mechoso, C. R., Wood, R., Weller, R., Bretherton, C. S., Clarke, A. D., Coe, H., Fairall, C., Farrar, J. T., Feingold,
407 G., Garreaud, R., Grados, C., McWilliams, J., de Szoeke, S. P., Yuter, S. E., and Zuidema, Z.: Ocean–cloud–
408 atmosphere–land interactions in the Southeastern Pacific: The VOCALS program, *B. Am. Meteorol. Soc.*, 95, 357-
409 375, doi:10.1175/BAMS-D-11-00246.1, 2013.

410 Meyer, K., Platnick, S., Oreopoulos, L., and Lee, D.: Estimating the direct radiative effect of absorbing aerosols
411 overlying marine boundary layer clouds in the southeast Atlantic using MODIS and CALIOP, *J. Geophys. Res.*
412 *Atmos.*, 118, 4801–4815, doi:10.1002/jgrd.50449, 2013.

413 Müller, D., Wandinger, U., and Ansmann, A.: Microphysical particle parameters from extinction and backscatter lidar
414 data by inversion with regularization: theory, *Appl. Optics*, 38, 2346-2357, 1999a.

415 Müller, D., Wandinger, U., and Ansmann, A.: Microphysical particle parameters from extinction and backscatter lidar
416 data by inversion with regularization: simulation, *Appl. Optics*, 38, 2358-2368, 1999b.

417 Müller, D., Hostetler, C. A., Ferrare, R. A., Burton, S. P., Chemyakin, E., Kolgotin, A., Hair, J. W., Cook, A. L.,
418 Harper, D. B., Rogers, R. R., Hare, R. W., Cleckner, C. S., Obland, M. D., Tomlinson, J., Berg, L. K., and Schmid,
419 B.: Airborne multiwavelength high spectral resolution lidar (HSRL-2) observations during TCAP 2012: vertical
420 profiles of optical and microphysical properties of a smoke/urban haze plume over the northeastern coast of the US,
421 *Atmos. Meas. Tech.*, 7, 3487-3496, doi:10.5194/amt-7-3487-2014, 2014.

422 Müller, D., Chemyakin, E., Kolgotin, A., Ferrare, R. A., Hostetler, C. A., and Romanov, A.: Automated, unsupervised,
423 inversion of multiwavelength lidar data with TiARA: assessment of retrieval performance of microphysical
424 parameters using simulated data, *Appl. Optics*, 58, 4981-5007, doi:10.1364/AO.58.004981, 2019.

425 Painemal, D., Kato, S., and Minnis, P.: Boundary layer regulation in the southeast Atlantic cloud microphysics during
426 the biomass burning season as seen by the A-train satellite constellation, *J. Geophys. Res. Atmospheres*, 119,
427 11,288-211,302, doi:10.1002/2014JD022182, 2014.

428 Peers, F., Francis, P., Fox, C., Abel, S. J., Szpek, K., Cotterell, M. I., Davies, N. W., Langridge, J. M., Meyer, K. G.,
429 Platnick, S. E., and Haywood, J. M.: Observation of absorbing aerosols above clouds over the south-east Atlantic
430 Ocean from the geostationary satellite SEVIRI – Part 1: Method description and sensitivity, *Atmos. Chem. Phys.*,
431 19, 9595–9611, <https://doi.org/10.5194/acp-19-9595-2019>, 2019.

432 Penner, J. E., Zhang, S. Y., and Chuang, C. C.: Soot and smoke aerosol may not warm climate, *J. Geophys. Res.*
433 *Atmospheres*, 108, 4657, doi:10.1029/2003JD003409, 2003.

434 Pistone, K., Zuidema, P., Wood, R., Diamind, M., da Silva, A. M., Ferrada, G., Saide, P. E., Ueyama, R., Ryoo, J.-
435 M., Pfister, L., Podolske, J., Noone, D., Bennett, R., Stith, E., Carmichael, G., Redemann, J., Flynn, C., LeBlanc,
436 S., Segal-Rozenhaimer, M., and Shinozuka, Y.: Exploring the elevated water vapor signal associated with the free
437 tropospheric biomass burning plume over the southeast Atlantic Ocean, *Atmos. Chem. Phys.*, 21, 9643-9668,
438 <https://doi.org/10.5194/acp-21-9643-2021>, 2021.

439 Pósfai, M., Simonics, R., Li, J., Hobbs, P. V., and Buseck, P. R.: Individual aerosol particles from biomass burning in
440 southern Africa: 1. Compositions and size distributions of carbonaceous particles, *J. Geophys. Res.*, 108, 8483,
441 doi:10.1029/2002JD002291, 2003.

442 Ramanathan, V., Crutzen, P. J., Kiehl, J. T., and Rosenfeld, D.: Aerosols, climate, and the hydrological cycle, *Science*,
443 294(5549), 2119-2124, doi:10.1126/science.1064034, 2001.

444 Randles, C. A., daSilva, A. M., Buchard, V., Colarco, P. R., Darmenov, A., Govindaraju, P., Smirnov, A., Holben, B.,
445 Ferrare, R. A., Hair, J., Shinozuka, Y., and Flynn, C. J.: The MERRA-2 aerosol reanalysis, 1980 onward. Part I:
446 System description and data assimilation evaluation, *J. Climate*, 30, 6823–6850, doi:10.1175/JCLI-D-16-0609.1,
447 2017.

448 Redemann, J., Wood, R., Zuidema, P., Doherty, S. J., Luna, B., LeBlanc, S. E., Diamond, M. S., Shinozuka, Y., Chang,
449 I. Y., Ueyama, R., Pfister, L., Ryoo, J.-M., Dobracki, A. N., da Silva, A. M., Longo, K. M., Kacenelenbogen, M.
450 S., Flynn, C. J., Pistone, K., Knox, N. M., Piketh, S. J., Haywood, J. M., Formenti, P., Mallet, M., Stier, P.,
451 Ackerman, A. S., Bauer, S. E., Fridlind, A. M., Carmichael, G. R., Saide, P. E., Ferrada, G. A., Howell, S. G.,
452 Freitag, S., Cairns, B., Holben, B. N., Knobelspiesse, K. D., Tanelli, S., L'Ecuyer, T. S., Dzambo, A. M., Sy, O. O.,
453 McFarquhar, G. M., Poellot, M. R., Gupta, S., O'Brien, J. R., Nenes, A., Kacarab, M., Wong, J. P. S., Small-
454 Griswold, J. D., Thornhill, K. L., Noone, D., Podolske, J. R., Schmidt, K. S., Pilewskie, P., Chen, H., Cochrane, S.
455 P., Sedlacek, A. J., Lang, T. J., Stith, E., Segal-Rozenhaimer, M., Ferrare, R. A., Burton, S. P., Hostetler, C. A.,
456 Diner, D. J., Seidel, F. C., Platnick, S. E., Myers, J. S., Meyer, K. G., Spangenberg, D. A., Maring, H., and Guo, L.:
457 An overview of the ORACLES (ObseRvations of Aerosols above Clouds and their intEractionS) project: aerosol-
458 cloud-radiation interactions in the southeast Atlantic basin, *Atmos. Chem. Phys.*, 21, 1507-1563, doi:10.5194/acp-
459 21-1507-2021, 2021.

460 Rogers, R. R., Hair, J. W., Hostetler, C. A., Ferrare, R. A., Obland, M. D., Cook, A. L., Harper, D. B., Burton, S. P.,
461 Shinozuka, Y., McNaughton, C. S., Clarke, A. D., Redemann, J., Russell, P. B., Livingston, J. M., and Kleinman,
462 L. I.: NASA LaRC airborne high spectral resolution lidar aerosol measurements during MILAGRO: observations
463 and validation, *Atmos. Chem. Phys.*, 9, 4811-4826, 2009.

464 Ryoo, J.-M., Pfister, L., Ueyama, R., Zuidema, P., Wood, R., Chang, I., and Redemann, J.: A meteorological
465 overview of the ORACLES (ObseRvations of Aerosols above CLouds and their intEractionS) campaign over the
466 southeastern Atlantic during 2016–2018: Part 1 – Climatology, *Atmos. Chem. Phys.*, 21, 16689–16707,
467 <https://doi.org/10.5194/acp-21-16689-2021>, 2021.

468 Sakaeda, N., Wood, R., and Rasch, P. J.: Direct and semidirect aerosol effects of southern African biomass burning
469 aerosol, *J. Geophys. Res. Atmospheres*, 116, D12205, doi:10.1029/2010JD015540, 2011.

470 Sawamura, P., Moore, R. H., Burton, S. P., Chemyakin, E., Müller, D., Kolgotin, A., Ferrare, R. A., Hostetler, C. A.,
471 Ziemba, L. D., Beyersdorf, A. J., and Anderson, B. E.: HSRL-2 aerosol optical measurements and microphysical
472 retrievals vs. airborne in situ measurements during DISCOVER-AQ 2013: an intercomparison study, *Atmos. Chem.*
473 *Phys.*, 17, 7229-7243, doi.org/10.5194/acp-17-7229-2017, 2017.

474 Schmid, B., Ferrare, R. A., Flynn, C., Elleman, R., Covert, D., Strawa, A., Welton, E., Turner, D., Jonsson, H.,
475 Redemann, J., Eilers, J., Ricci, K., Hallar, A. G., Clayton, M., Michalsky, J., Smirnov, A., Holben, B., and Barnard,
476 J. : How well do state-of-the-art techniques measuring the vertical profile of tropospheric aerosol extinction
477 compare? *J. Geophys. Res.*, 111, D05S07, doi:10.1029/2005JD005837, 2006.

478 She, C. Y., Alvarez II, R. J., Caldwell, L. M., and Krueger, D. A.: High-spectral-resolution Rayleigh-Mie lidar
479 measurement of aerosol and atmospheric profiles, *Opt. Lett.*, 17, 541-543, 1992.

480 Shingler, T., Crosbie, E., Ortega, A., Shiraiwa, M., Zuend, A., Beyersdorf, A., Ziemba, L., Anderson, B., Thornhill,
481 L., Perring, A. E., Schwarz, J. P., Campazano-Jost, P., Day, D. A., Jimenez, J. L., Hair, J. W., Mikoviny, T.,
482 Wisthaler, A., & Sorooshian, A.: Airborne characterization of subsaturated aerosol hygroscopicity and dry refractive

483 index from the surface to 6.5km during the SEAC⁴RS campaign, *J. Geophys. Res.*, 121(8), 4188-4210,
484 <https://doi.org/10.1002/2015JD024498>, 2016.

485 Shinozuka, Y., Saide, P. E., Ferrada, G. A., Burton, S. P., Ferrare, R. A., Doherty, S. J., Gordon, H., Longo, K., Mallet,
486 M., Feng, Y., Wang, Q., Cheng, Y., Dobracki, A., Freitag, S., Howell, S. G., LeBlanc, S., Flynn, C., Segal-
487 Rozenhaimer, M., Pistone, K., Podolske, J. R., Stith, E. J., Bennett, J. R., Carmichael, G. R., da Silva, A.,
488 Govindaraju, R., Leung, R., Zhang, Y., Pfister, L., Ryoo, J.-M., Redemann, J., Wood, R., and Zuidema, P.: Modeling
489 of the smoky troposphere of the southeast Atlantic: a comparison to ORACLES airborne observations from
490 September of 2016, *Atmos. Chem. Phys.*, 20, 11491-11526, doi:10.5194/acp-20-11491-2020, 2020.

491 Shipley, S. T., Tracy, D. H., Eloranta, E. W., Tauger, J. T., Stroga, J. T., Roesler, F. L., and Weinman, J. A.: High
492 spectral resolution lidar to measure optical scattering properties of atmospheric aerosols. 1. Theory and
493 instrumentation, *Appl. Optics*, 22, 3716-3724, 1983.

494 Stein, A.F., Draxler, R. R., Rolph, G. D., Stunder, B. J. B., Cohen, M. D., and Ngan, F.: NOAA's HYSPLIT
495 atmospheric transport and dispersion modeling system, *B. Am. Meteorol. Soc.*, 96, 2059-2077, doi:10.1175/BAMS-
496 D-14-00110.1, 2015.

497 Veselovskii, I., Kolgotin, A., Grazianov, V., Müller, D., Wandinger, U., and Whiteman, D. N.: Inversion with
498 regularization for the retrieval of tropospheric aerosol parameters from multi-wavelength lidar sounding, *Appl.*
499 *Optics*, 41, 3685-3699, 2002.

500 Wilcox, E. M.: Stratocumulus cloud thickening beneath layers of absorbing smoke aerosol, *Atmos. Chem. Phys.*, 10,
501 11769-11777, doi:10.5194/acp-10-11769-2010, 2010.

502 Wilcox, E. M.: Direct and semi-direct radiative forcing of smoke aerosols over clouds, *Atmos. Chem. Phys.*, 12, 139-
503 149, doi:10.5194/acp-12-139-2012, 2012.

504 Wu, H., Taylor, J. W., Szpek, K., Langridge, J. M., Williams, P. I., Flynn, M., Allan, J. D., Abel, S. J., Pitt, J., Cotterell,
505 M. I., Fox, C., Davies, N. W., Haywood, J., and Coe, H.: Vertical variability of the properties of highly aged biomass
506 burning aerosol transported over the southeast Atlantic during CLARIFY-2017, *Atmos. Chem. Phys.*, 20, 12697-
507 12719, <https://doi.org/10.5194/acp-20-12697-2020>, 2021.

508 Xu F., Gao, L., Redemann, J., Flynn C.J., Espinosa, W.R., da Silva, A.M., Stamnes, S., Burton, S.P., Liu, X., Ferrare,
509 R., Cairns, B. and Dubovik, O.: A Combined Lidar-Polarimeter Inversion Approach for Aerosol Remote Sensing
510 Over Ocean, *Front. Remote Sens*, 2:620871, doi: 10.3389/frsen.2021.620871, 2021.

511 Yamaguchi T, Feingold, G., Kazil, J., and McComiskey, A.: Stratocumulus to cumulus transition in the presence of
512 elevated smoke layers. *Geophys. Res. Lett.*, 42: 10478-10485, 2015.

513 Zhang, J. and Zuidema, P.: The diurnal cycle of the smoky marine boundary layer observed during August in the
514 remote southeast Atlantic, *Atmos. Chem. Phys.*, 19, 14493-14516, <https://doi.org/10.5194/acp-19-14493-2019>,
515 2019.

516 Zhang Z., Meyer, K., Yu, H., Platnick, S., Colarco, P. R., Liu, Z., and Oreopoulos, L.: Shortwave direct radiative
517 effects of above-cloud aerosols over global oceans derived from 8 years of CALIPSO and MODIS observations,
518 *Atmos. Chem. Phys.*, 16, 2877-2900, doi:10.5194/acp-16-2877-2016, 2016.

519 Zhang, X., Mao, M., Yin, Y., and Tang, S.: The absorption Ångström exponent of black carbon with brown coatings:
520 effects of aerosol microphysics and parameterization, *Atmos. Chem. Phys.*, 20, 9701-9711, doi:10.5194/acp-20-
521 9701-2020, 2020.

522 Zuidema, P., Redemann, J., Haywood, J., Wood, R., Piketh, S., Hipondoka, M., and Formenti, P.: Smoke and clouds
523 above the southeast Atlantic, *B. Am. Meteorol. Soc.*, 97, 1131-1135, doi:10.1175/BAMS-D-15-00082.1, 2016.

524 Zuidema, P., Sedlacek III, A. J., Flynn, C., Springston, S., Delgadillo, R., Zhang, J., Aiken, A. C., Koontz, A., and
525 Muradyan, P.: The Ascension Island boundary layer in the remote Southeast Atlantic is often smoky, *Geophys. Res.*
526 *Lett.*, 45, 4456-4465, doi:10.1002/2017GL076926, 2018.

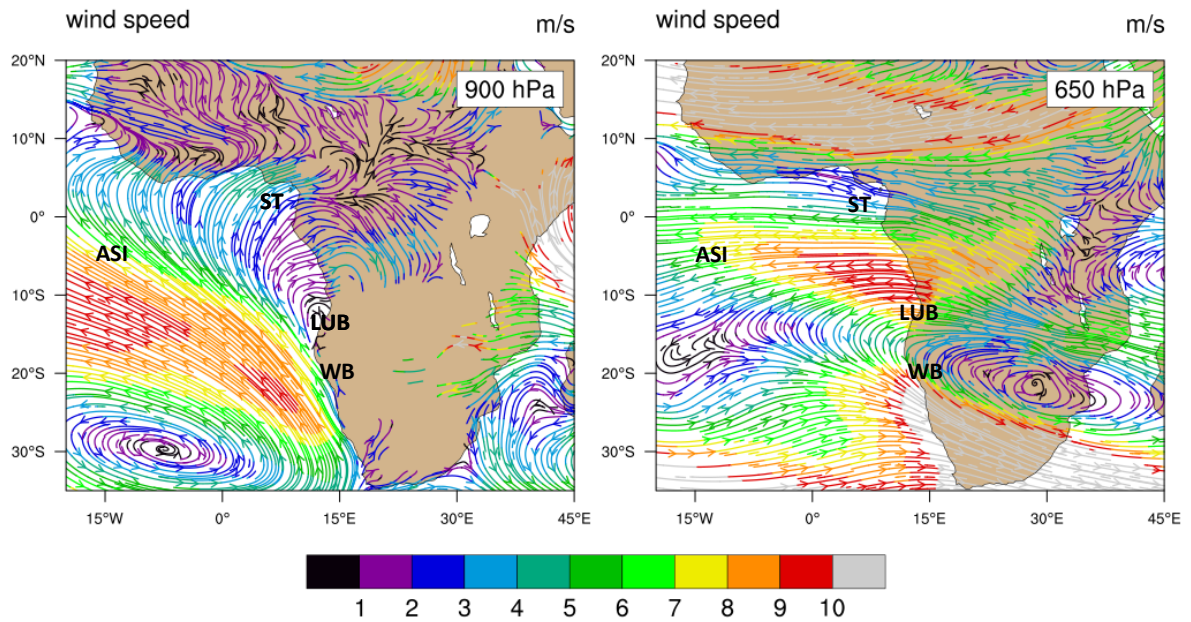
527

528
529
530

Table 1: Averaging area, flight time periods, the duration over water and number of HYSPLIT backward trajectories, and number of HSRL-2 profiles in each grid box used in the study.

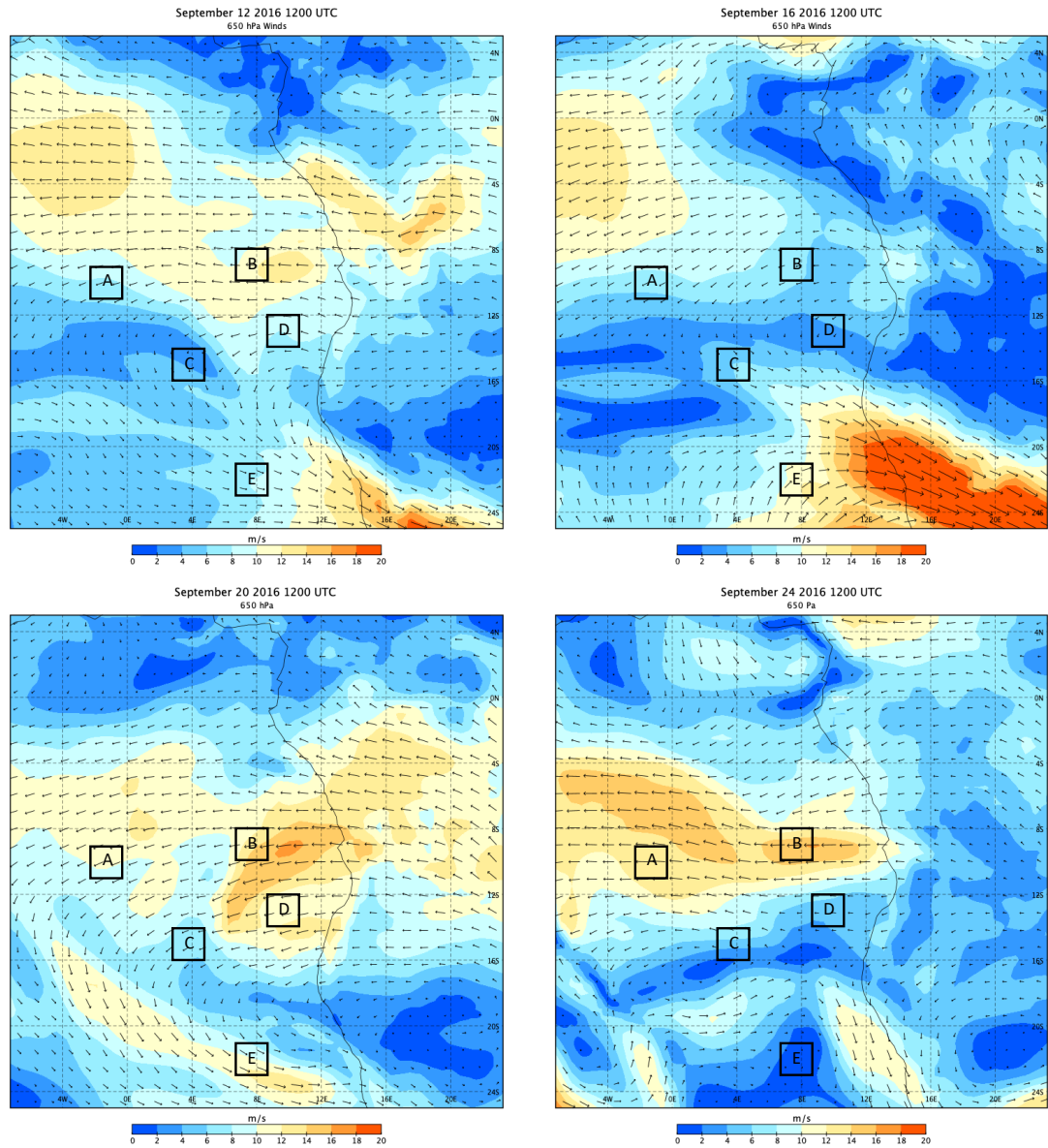
Box	Averaging Area	Averaging Days	Time of Day	Duration in Hours Over Water at 3.5 km	Number of Profiles
A	11° S-9° S; 1° W-1° E	9/12, 16	11:00 UTC	44.3±7.0 (N = 19)	50
B	10° S-8° S; 8° E-10° E	9/12, 16, 18	10:00 UTC	14.9±4.5 (N = 27)	56
C	16° S-14° S; 4° E-6° E	9/12, 16	13:00 UTC	40.4±7.2 (N = 19)	51
D	14° S-12° S; 10° E-12° E	9/18, 24	09:00 UTC	5.5±2.0 (N = 27)	46
E	23° S-21° S; 8° E-10° E	9/20, 22	14:00 UTC	-	36

531



533
 534
 535
 536
 537
 538

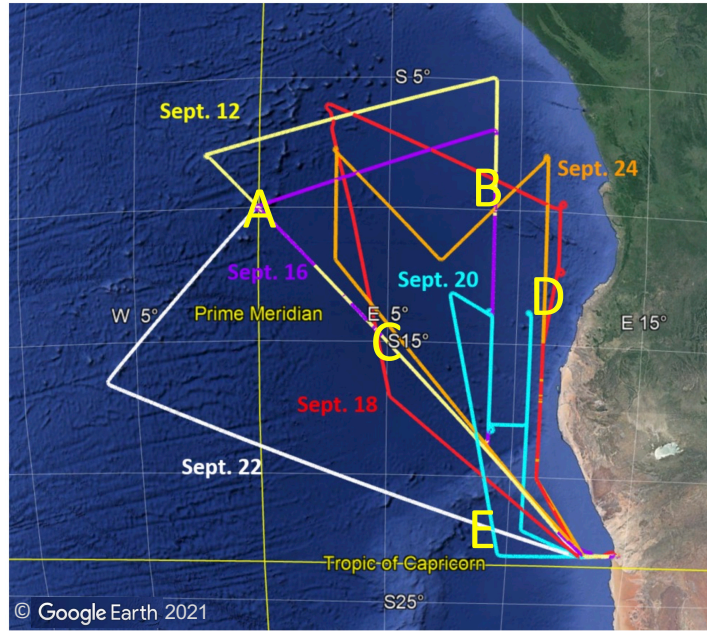
Figure 1: MERRA-2 monthly mean reanalysis of 900 and 650 hPa streamlines for September 2016. Stations marked are Ascension Island (ASI), Lubango (LUB), a long-term AERONET site at 2 km elevation, and Walvis Bay (WB), where ER-2 flights originated from during the September 2016 ORACLES IOP. Flights in August 2017 and September/October 2018 originated from São Tomé (ST).



539
540
541
542

Figure 2: MERRA-2 reanalysis of 650 hPa winds at 1200 UTC on September 12, 16, 20, 24, 2016. Grid boxes in the study are marked with letters.

543
544

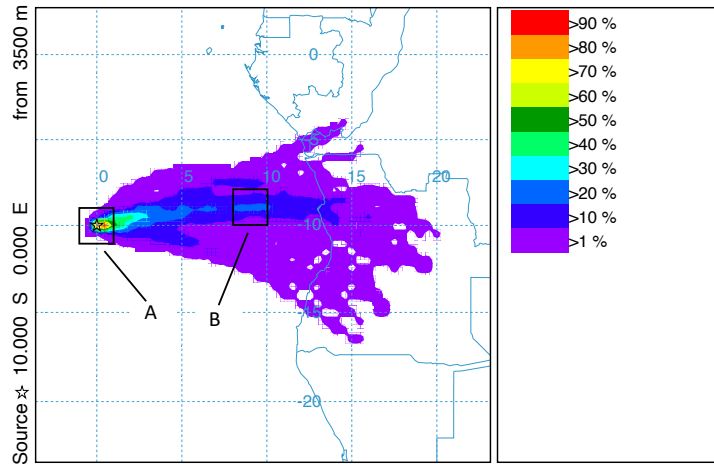


545
546

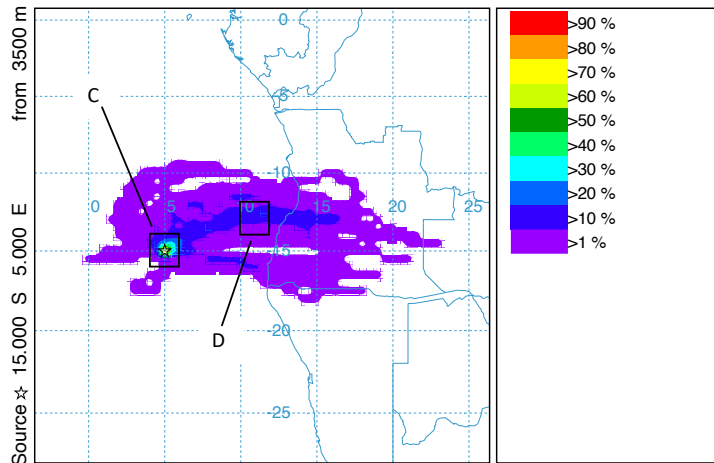
547
548
549

Figure 3: HSRL-2 science data flight tracks during the September 2016 IOP. Letters refer. to the grid boxes identified in Fig. 2 (© Google Earth).

NOAA HYSPLIT MODEL - TRAJECTORY FREQUENCIES
 # trajs passing through grid sq./# trajectories (%) 0 m and 99999 m
 Integrated from 1200 24 Sep to 1800 10 Sep 16 (UTC) [backward]
 Freq Calculation started at 0000 00 00 (UTC)



NOAA HYSPLIT MODEL - TRAJECTORY FREQUENCIES
 # trajs passing through grid sq./# trajectories (%) 0 m and 99999 m
 Integrated from 1200 24 Sep to 1800 10 Sep 16 (UTC) [backward]
 Freq Calculation started at 0000 00 00 (UTC)



551
 552
 553
 554
 555
 556

Figure 4: Frequency distribution of 48 h backward trajectories of air parcels arriving at 3500 m above the centers of grid boxes A and C over the time period of the campaign. Grid boxes B and D are upstream of grid boxes A and C, respectively.

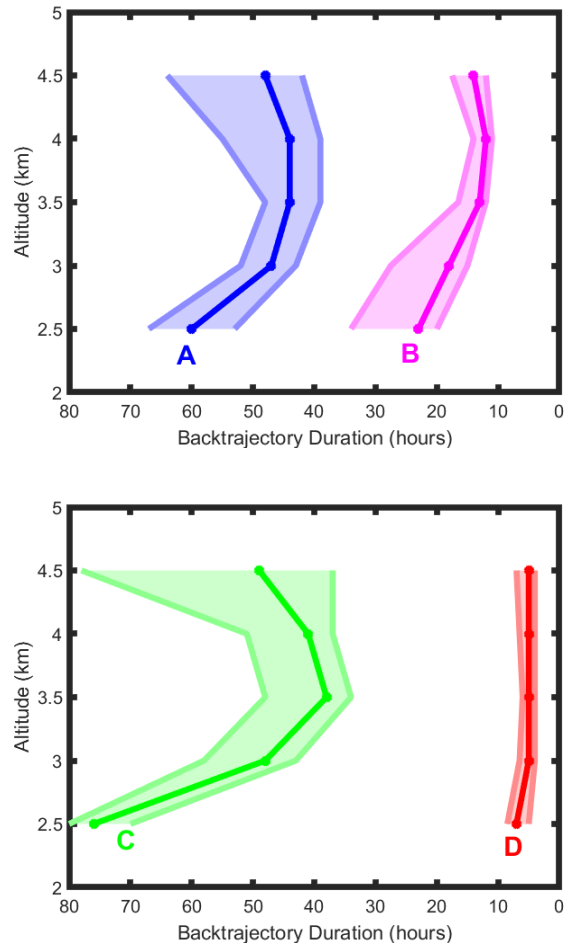
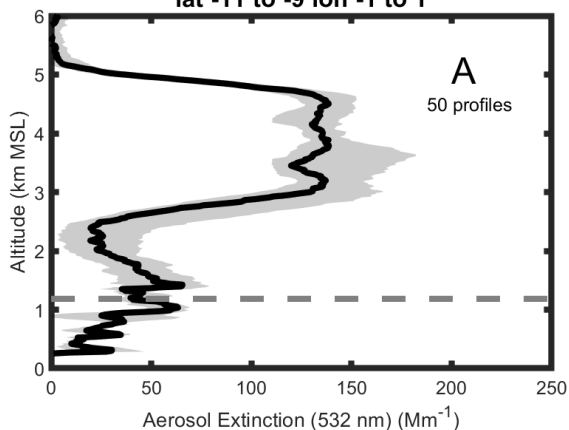


Figure 5: Duration of time spent over water of air parcels arriving at grid boxes marked on the figure. Solid lines are median values, and the shaded portion are the range of the 75th and 25th percentile. The number of trajectories used for the calculation are in Table 1. Trajectory hours are shown in reverse to correspond to the map in Fig. 4.

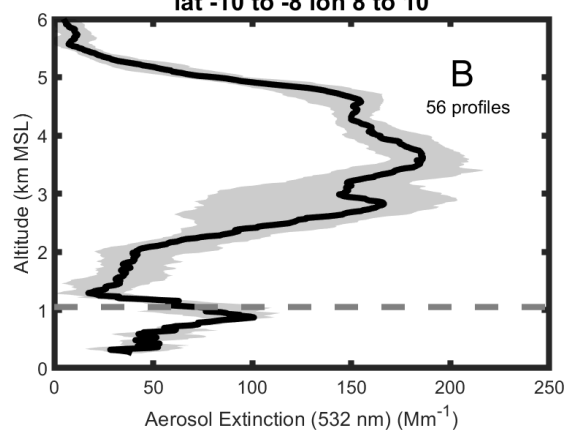
558
 559
 560
 561
 562
 563
 564

565

Aerosol Extinction 532 nm Sept. 12,16, 2016
lat -11 to -9 lon -1 to 1

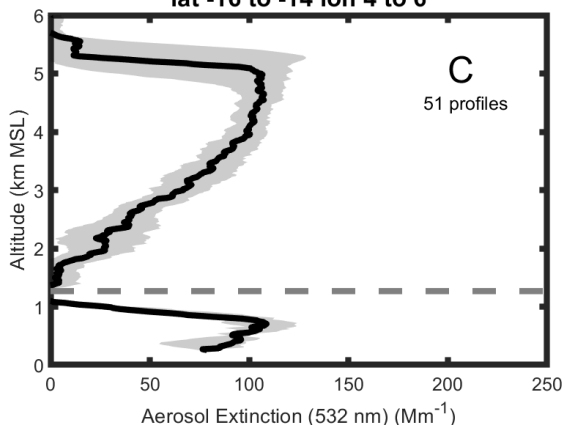


Aerosol Extinction 532 nm Sept. 12,16,18 2016
lat -10 to -8 lon 8 to 10

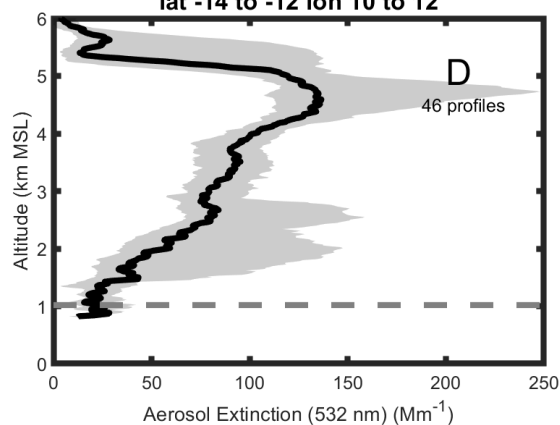


566

Aerosol Extinction 532 nm Sept. 12,16 2016
lat -16 to -14 lon 4 to 6

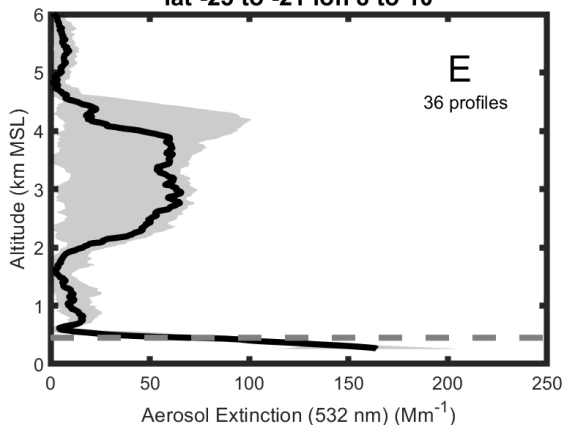


Aerosol Extinction 532 nm Sept. 18,24 2016
lat -14 to -12 lon 10 to 12



567

Aerosol Extinction 532 nm Sept. 20,22 2016
lat -23 to -21 lon 8 to 10



568

569

570

571

572

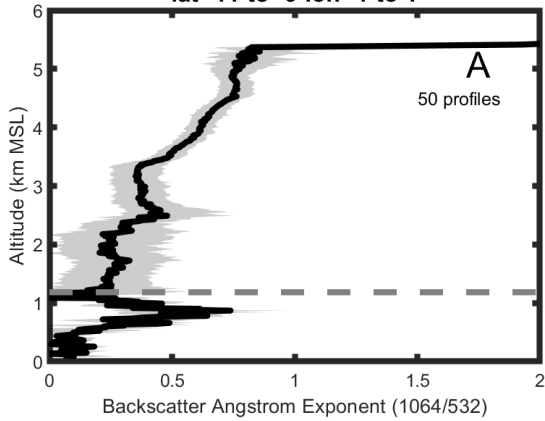
573

574

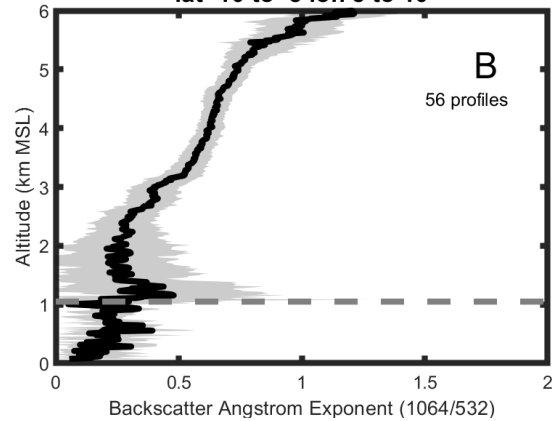
Figure 6: Average vertical profiles of the aerosol extinction coefficient at 532 nm in grid boxes A (upper left), B (upper right), C (middle left), D (middle right) and E (lower left). The averaging area, dates of flights and total number of 1 min profiles are also shown. The dark line represents the median value and grey shades contain the 25th to 75th percentiles. Dashed line refers to the mean cloud top height.

575

Backscatter Ang. Expo. 1064/532 Sept. 12,16, 2016
lat -11 to -9 lon -1 to 1

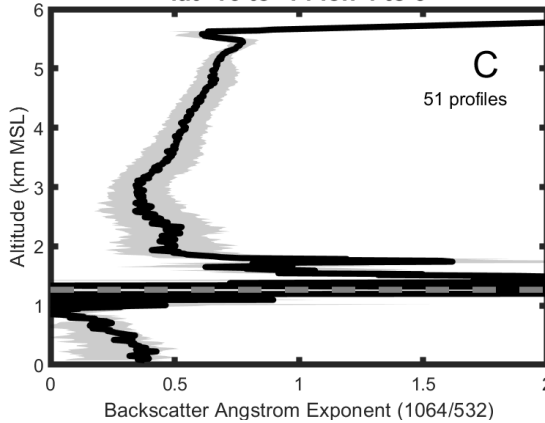


Backscatter Ang. Expo. 1064/532 Sept. 12,16,18 2016
lat -10 to -8 lon 8 to 10

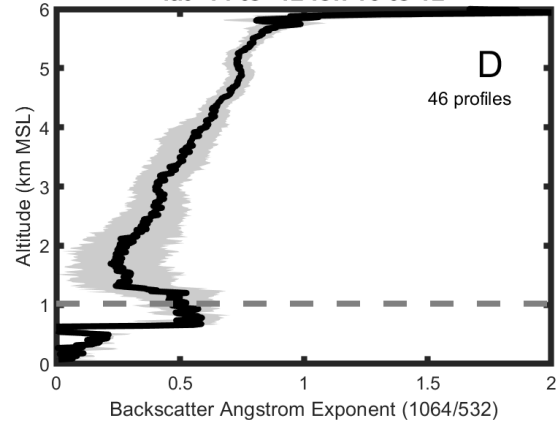


576

Backscatter Ang. Expo. 1064/532 Sept. 12,16 2016
lat -16 to -14 lon 4 to 6

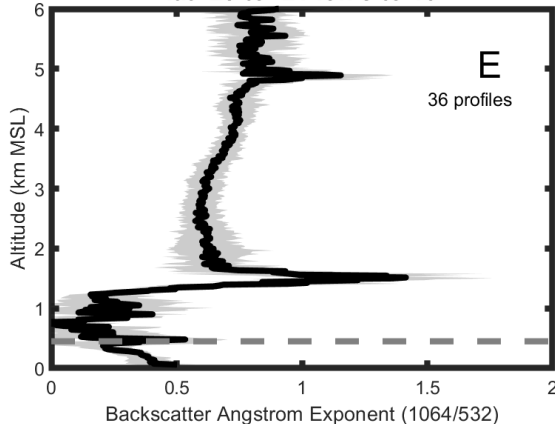


Backscatter Ang. Expo. 1064/532 Sept. 18,24 2016
lat -14 to -12 lon 10 to 12



577

Backscatter Ang. Expo. 1064/532 Sept. 20,22 2016
lat -23 to -21 lon 8 to 10



578

579

580

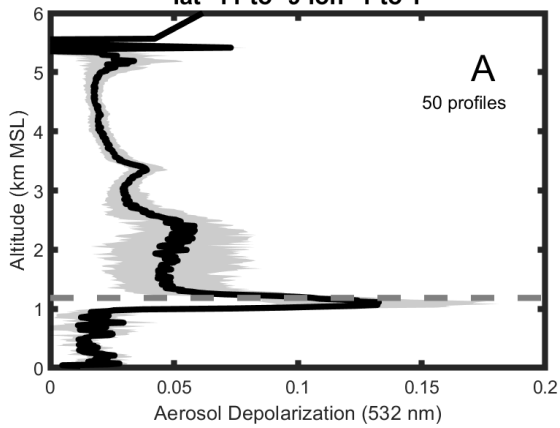
581

582

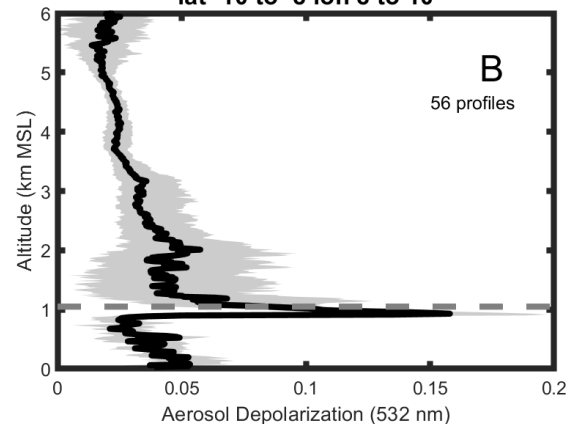
Figure 7: As in Fig. 6 but for the wavelength-dependent backscatter Ångström exponent between 1064 and 532 nm.

583

**Aerosol Depolarization 532 nm Sept. 12,16, 2016
lat -11 to -9 lon -1 to 1**

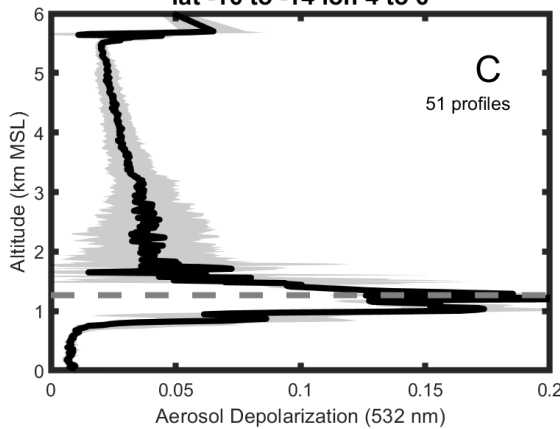


**Aerosol Depolarization 532 nm Sept. 12,16,18 2016
lat -10 to -8 lon 8 to 10**

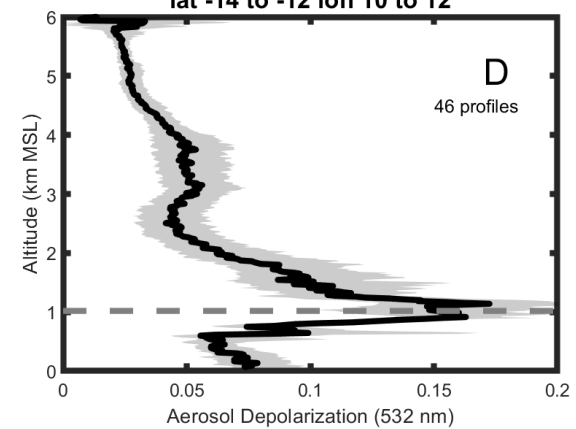


584

**Aerosol Depolarization 532 nm Sept. 12,16 2016
lat -16 to -14 lon 4 to 6**

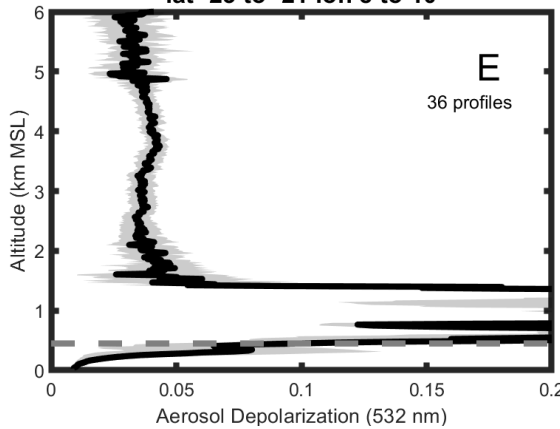


**Aerosol Depolarization 532 nm Sept. 18,24 2016
lat -14 to -12 lon 10 to 12**



585

**Aerosol Depolarization 532 nm Sept. 20,22 2016
lat -23 to -21 lon 8 to 10**



586

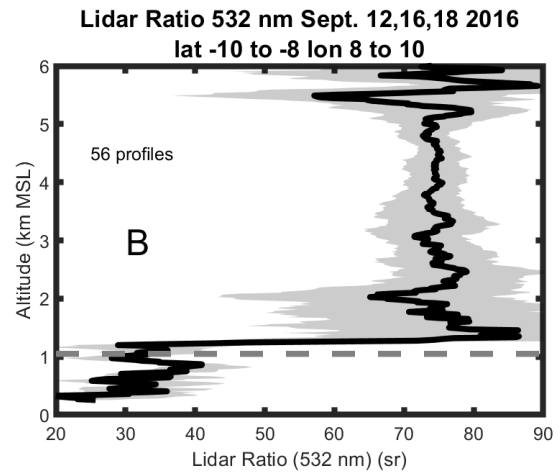
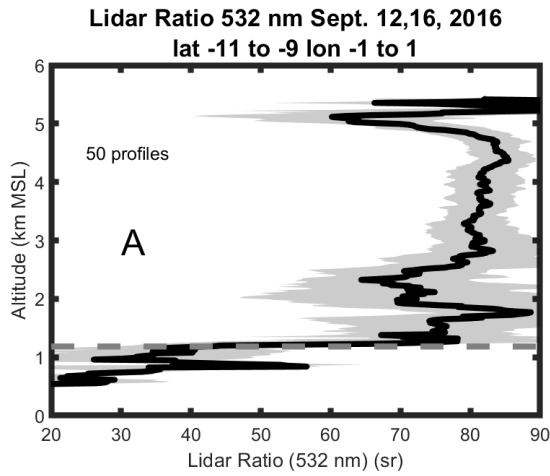
587

588

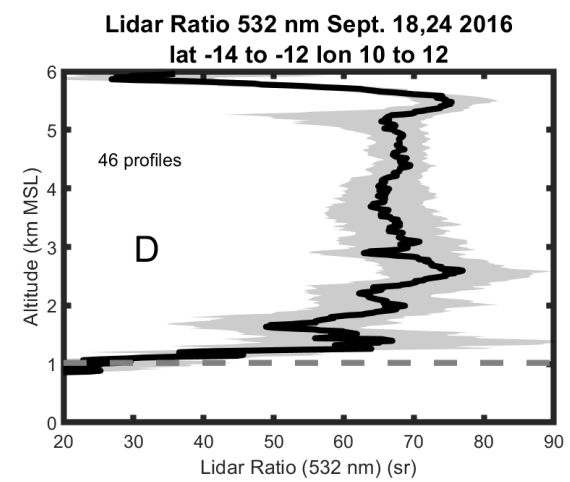
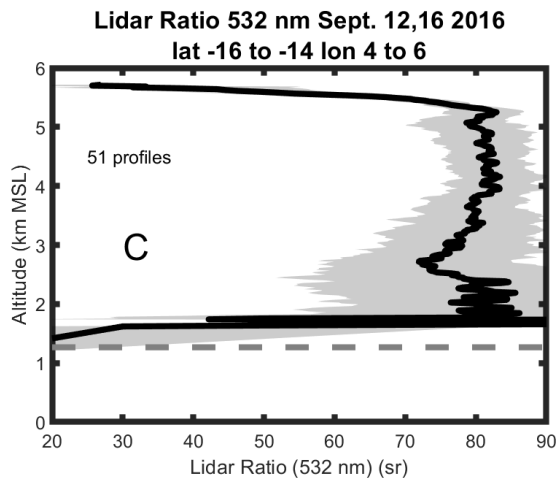
589

Figure 8: As in Fig. 6 but for the aerosol depolarization at 532 nm.

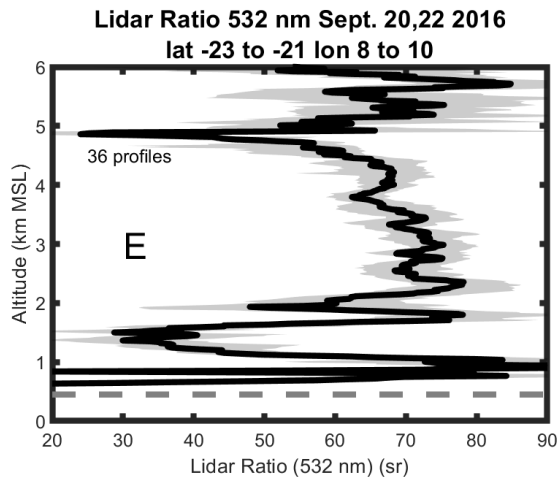
590



591



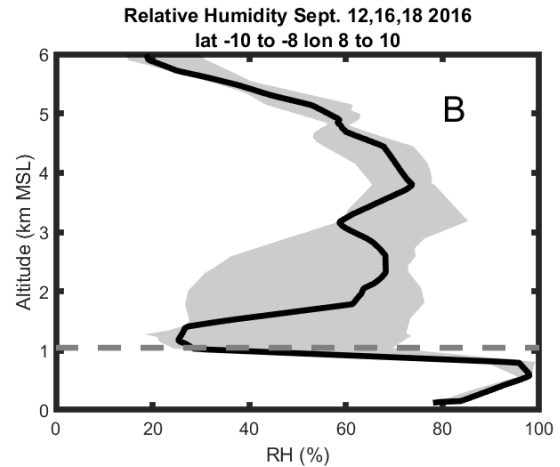
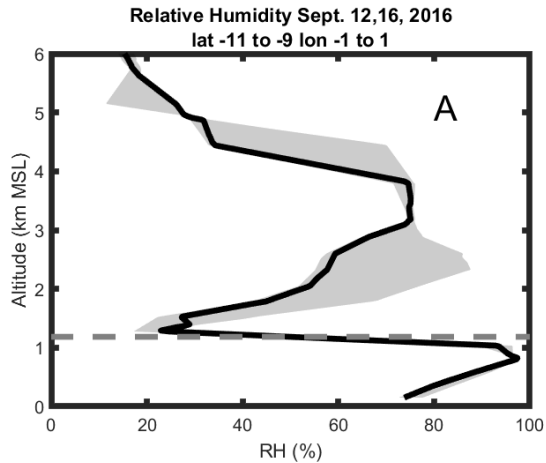
592



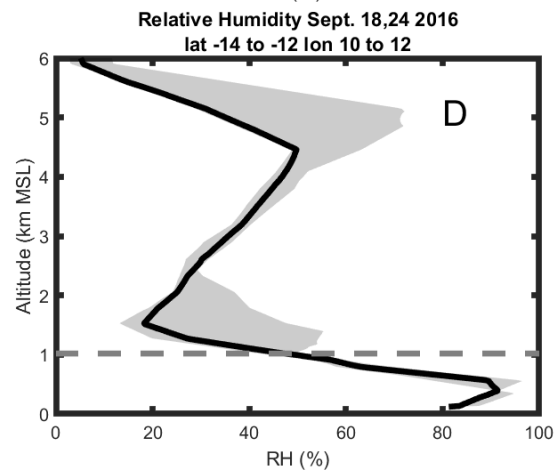
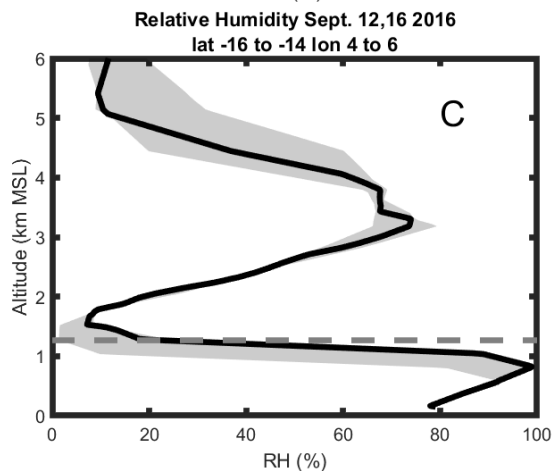
593
594
595
596

Figure 9: As in Fig. 6 but for the lidar ratio at 532 nm.

597



598



599
600
601
602
603
604
605
606

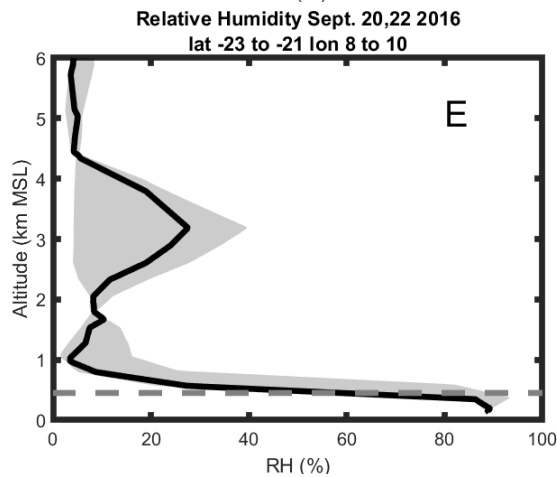
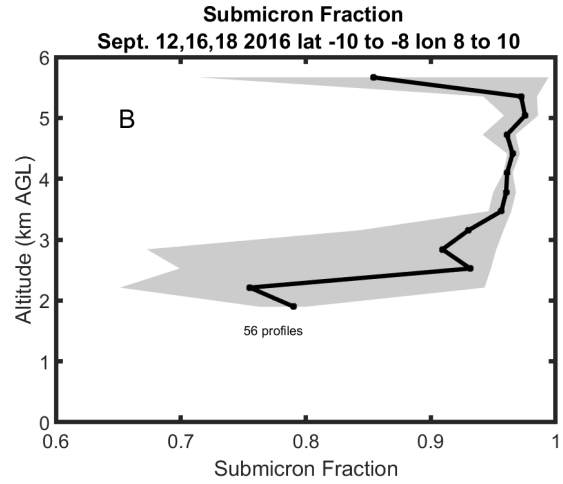
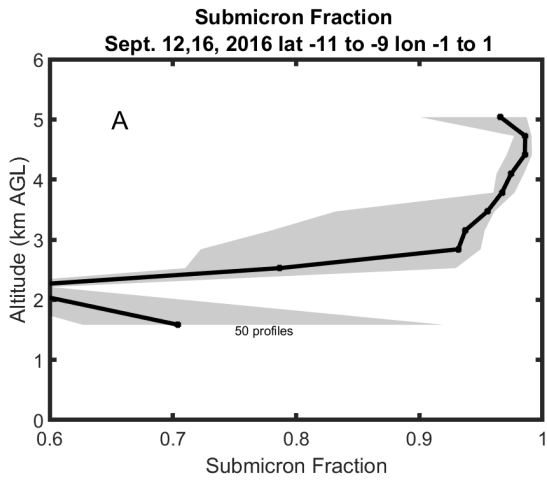
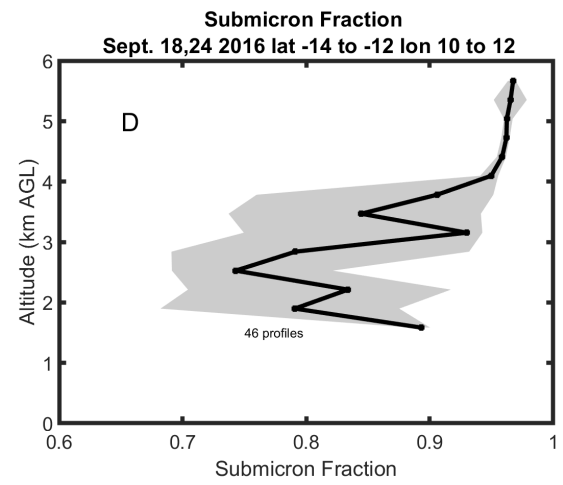
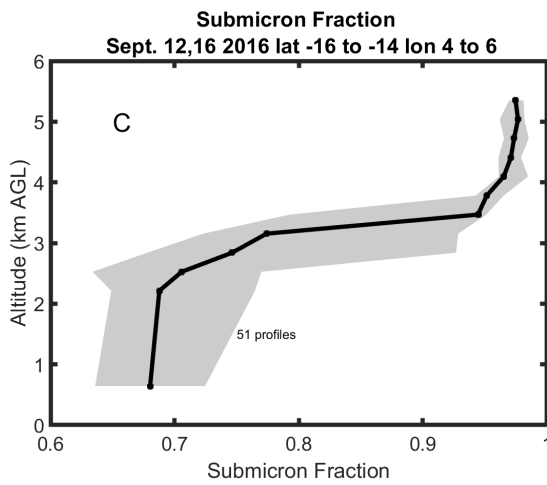


Figure 10: Relative Humidity (%) in grid boxes A (upper left), B (upper right), C (middle left), D (middle right) and E (lower left) from MERRA-2 reanalysis corresponding to the HSRL-2 profiles shown in Figs. 6-9. The dark line represents the median value and grey shades contain the 25th to 75th percentiles. Dashed line refers to the mean cloud top height.

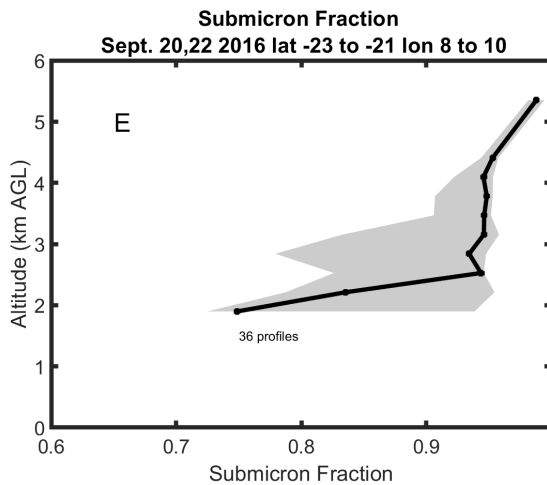
607



608



609



610

611

612

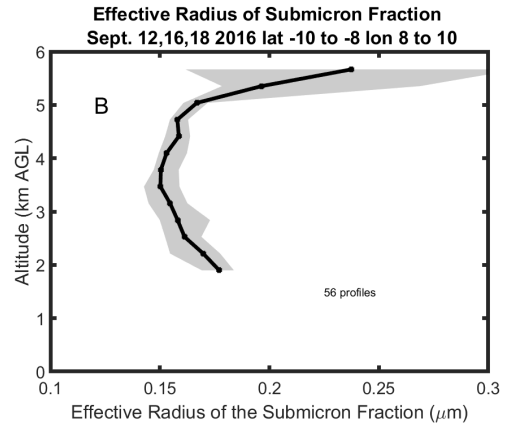
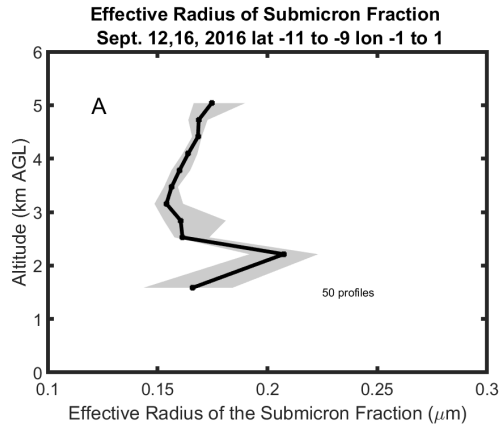
613

614

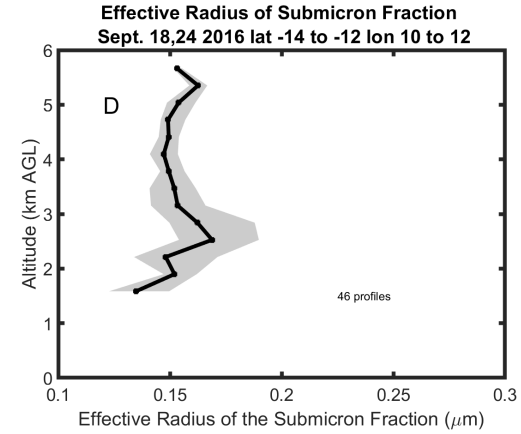
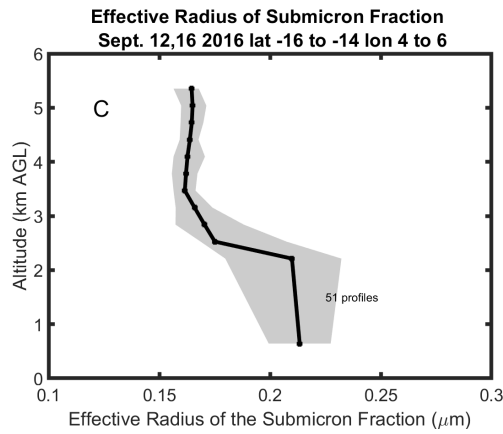
615

Figure 11: Average vertical profiles of the submicron fraction in grid boxes A (upper left), B (upper right), C (middle left), D (middle right) and E (lower left). The averaging area, dates of flights and total number of one-minute profiles in the average are also shown. The dark line represents the median value and grey shades contain the 25th to 75th percentiles.

616



617



618

619

620

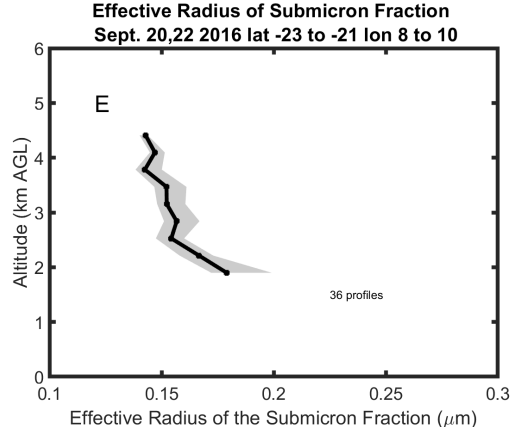


Figure 12: As in Fig. 11 but for the effective radius of the submicron fraction.